

Strain rate effects at tensile loading of single crystal Cu nano-wires

Solveig Melin, Aylin Ahadi

solveig.melin@mek.lth.se

Abstract

It is well-known and experimentally confirmed that the mechanical response to loading of small enough structures differs from what applies to the macro-scale. This is valid for structures of linear measures at the nano-scale, typically below about 50nm. In addition to pure size effects also the crystallographic orientation becomes important at this scale. This study demonstrates the mechanical response to displacement controlled tensile loading of solid nano-sized fcc single-crystal Cu beams of square shaped cross sections. The investigation was performed through 3D molecular dynamic simulations using the free-ware LAMMPS. Two different crystal orientations and different loading rates were considered. Deformations and stress-strain curves were obtained and the necking behavior was studied in detail.

1 Introduction

Fragmentation of metals due to high strain rate loading is a well-recognized phenomenon at the global scale. The fragmentation pattern is affected by inertia as well as by stress waves traveling within the specimen. Also material properties, both the elastic and the plastic responses, are dependent on strain rate. This is true at the global scale but applies also at the nano scale. For nano-sized components further complications emerge because the material properties become size dependent for small enough components. This size effect is experimentally demonstrated; cf. e.g. [1, 2]. Further, from experiments Kraft and co-workers concluded that it is the relative number of surface atoms as compared to number of bulk atoms that influences the mechanical properties, cf. [3, 4, 5]. This is due to that surfaces imply the absence of atomic bonds, leaving surface atoms in energy states deviating from those of bulk atoms. The redistribution of the electron density close to a surface affects the inter-atomic bonding forces and, thereby, both the local load carrying capacity and the load distribution within the structure, cf. e.g. [6, 7, 8, 9]. Such an influence is not noticed, and thus not taken into account, at the macro-scale since the share of surface atom is small so that the mechanical response is ruled by the bulk atoms. Another aspect that has to be taken into account at the nano-scale

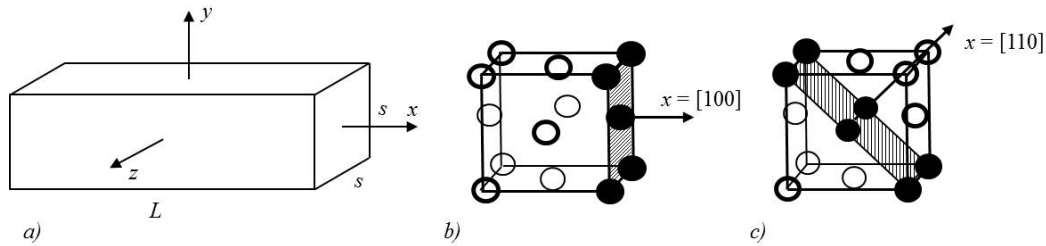


Figure 1: a) Beam configuration and coordinate system. b),c) Crystallographic orientations $[100]$ and $[110]$, respectively.

is the local crystallographic orientation, determining the elastic properties as well as defining pertinent slip plane directions determining the plastic response, cf. [7]. For components at the global scale normally there is an even spread of crystallographic orientations between the grains, eliminating directional dependence. In this paper the strain rate dependence at tensile loading of beams of single-crystal Cu of two different crystallographic orientations and three different cross section sizes is investigated. To accomplish this, 3D molecular dynamics simulations have been performed. As expected, both geometry and crystal orientation influences the mechanical response.

2 Statement of the problem

2.1 Model geometry

Beams of single crystal fcc Cu, of length L and quadratic cross section with side length s , are loaded under tension in their length direction x , cf. Fig. 1a) where a coordinate system (x, y, z) is introduced. The beam length is kept constant equal to $L = 300a_0$, with $a_0 = 3.615 \text{ \AA}$ denoting the lattice constant for Cu. Three different cross section sizes are investigated, with $s = 6a_0$, $12a_0$ and $18a_0$.

Two different crystallographic orientations have been considered. For the first, referred to as the $[100]$ -orientation, Fig. 1b), $[100]$, $[010]$ and $[001]$ coincide with the x -, y - and z -directions, respectively. For the second orientation, referred to as the $[110]$ -orientation, Fig. 1c), $[110]$, $[-110]$ and $[001]$ coincide with the x -, y - and z -directions, respectively.

2.2 Molecular dynamics

The molecular dynamics free-ware LAMMPS, [10] has been used for the simulations and the atomic images are produced using OVITO developed by [11].

The beam is built from the repetition of Cu fcc unit cells and the interaction between the Cu atoms is described by an EAM-potential, giving the potential energy of an atom. This potential consists of one pair-wise repulsive part and one N -body attractive part, with a cut-off radii, cf. [12, 13]. The potential energy, of atom i of

type α is given by Eq. (1):

$$E_i^\alpha = f_\alpha \left(\sum_{i \neq j} \rho_\beta (r^{ij}) \right) + \frac{1}{2} \sum_{i \neq j} \varphi_{\alpha\beta} (r^{ij}) \quad (1)$$

where α and β are two types of atoms, r^{ij} is the distance between atoms i and j , $\varphi_{\alpha\beta}$ is a pair-wise potential function, ρ_β is the contribution to the electron charge density from atom j of type β at the location of atom i , and f_α is an embedding function that represents the energy required to place atom i of type α into the electron cloud. Here only one type of atoms is present so that α and β are the same. In this study the potential file named Cu-u3.eam, given in LAMMPS and developed by [14] have been used.

The per-atom stresses, σ_{kl}^i , $k, l = x, y, z$, of atom i are in LAMMPS calculated as

$$\sigma_{kl}^i = -\frac{1}{V^i} \left(m^i v_k^i v_l^i + \sum_j F_k^{ij} r_l^{ij} \right) \quad (2)$$

Here V^i is the atomic volume, assumed equal for all atoms and determined at the start of the simulation after an initial relaxation of the system to find the equilibrium state. Further, m^i is the atomic mass, v_k^i and v_l^i the velocities of atom i in the k - and l -directions, F_k^{ij} the force in the k -direction between atoms i and j , and the distance in the l -direction between atoms i and j .

A NVT-ensemble is generated and the temperature T is kept constant equal to $T = 0.01\text{K}$ by a Nosé-Hoover thermostat according to [15]. Initially the atomic ensemble is relaxed to its equilibrium state for 5000 time steps, corresponding to 25ps. Thereafter an axial elongation is effectuated by applying a constant velocity v_{end} in the $+x$ - and $-x$ -directions to four unit cells at each end of the beam at the same time as the atoms of these cells are restricted from movements in the y - and z -directions. Thus clamped boundary conditions are mimicked. All atoms in between these end cells are free to move without constraints. The displacement controlled load is applied with time step $\Delta t = 5\text{fs}$ and the end velocities investigated are $v_{end} = Mv_0$, with $v_0 = a_0/400/\text{ps}$ and $M = 1, 2, 4, 6, 8$. The results are evaluated using the centro-symmetry parameter CSP according to [16], as being a measure of the instantaneous lattice disorder. The centro-symmetry parameter for an atom is defined according to Eq. (3),

$$CSP = \sum_{i=1}^{N/2} |R_i + R_{i+N/2}|^2 \quad (3)$$

where the N is the number of nearest neighbors in the surrounding lattice, equal to 12 for a fcc lattice. R_i and $R_{i+N/2}$ are the vectors corresponding to pairs of opposite nearest-neighbors in the lattice. The value of the CSP signals whether an atom is part of a perfect lattice, a local defect (a vacancy, partial dislocation or a stacking fault), or part of a free surface. Commonly used CSP values for different situations in fcc lattices are shown in Table 6, cf. [17] for the values marked by *. However, for atoms situated along edges or at corners, the CSP values reach much higher values

than at a free surface. For the beam geometry with crystallographic orientations [100] and [110] as studied here, the pertinent CSP values for surface atoms together with edge- and corner-atoms are inserted in Table 6 and marked by Δ , cf. [18].

Lattice structure	CSP
* Ideal fcc structure	$CSP < 3$
* Partial dislocation	$3 < CSP < 5$
* Stacking fault	$5 < CSP < 9$
* Surface atoms	$9 < CSP < 20$
Δ Surface atoms [100]	$9 < CSP \leq 21$
Δ Surface atoms [110]	$9 < CSP \leq 25$
Δ Edge- and corner atoms [100]	$CSP > 21$
Δ Edge- and corner atoms [110]	$CSP > 25$

Table 6: CSP values for fcc lattices; * after [17], Δ after [18].

3 Results and Discussion

3.1 Rate dependence of plasticity initiation and rupture

During loading of the beams, the deformations are monitored in detail. The initiation of plasticity, i.e. the time at the first slip event, is denoted t_i , and the strain at this event is denoted ε_i . At subsequent loading rupture of the beam eventually occurs at time t_{1f} , when the applied axial strain is ε_{1f} . In some cases rupture is found to occur more than once. The time at which this eventual second rupture occurs, resulting in three separate parts, is denoted t_{2f} . The times t_i , t_{1f} and t_{2f} are plotted in Fig. 2 for both orientations and all investigated velocities.

In Tables 7-9 the values of ε_i and ε_{1f} are found for cross section side lengths $s = 6a_0$, $12a_0$ and $18a_0$, respectively, for all investigated velocities and for both crystallographic orientations. The time delay to an eventual second rupture, $\Delta t = t_{2f} - t_{1f}$, is also given. The results are plotted in Fig. 3 for clarity.

As seen from the Tables 7-9 and Fig. 3, the plastic initiation strain ε_i is almost independent of size s . On the other hand, the dependence of ε_i on v_{end} is obvious. It seems that there is an overall tendency for ε_i to attend values at two different strain levels; very roughly $\varepsilon_i \approx 0.09$ for the lower end velocities and $\varepsilon_i \approx 0.03$ for the higher for the [100]-orientation. Similarly, $\varepsilon_i \approx 0.07$ at the lower end velocities and $\varepsilon_i \approx 0.02$ at the higher for the [110]-orientation. In both cases there is a drop of about a factor of 3, with the transition around $v_{end} = 4v_0$.

For the [100]-orientation the strain at first rupture, ε_{1f} , first increases with v_{end} , but beyond $v_{end} = 2v_0$ it decreases again. This coincides with the emergence of a second rupture at time t_{2f} , cf. Tables 8-10 and Fig. 2.

Orientation	[100]			[110]		
	ε_i	ε_{1f}	Second rupture, Δt	ε_{1f}	ε_{1f}	Second rupture, Δt
1	0.0936	0.1291	no	0.0671	0.1326	no
2	0.0949	0.1479	0.525	0.0684	0.1300	0.425
4	0.0855	0.1300	0.100	0.0547	0.1146	0.100
6	0.0410	0.0975	0.150	0.0231	0.0949	0.075
8	0.0308	0.0752	0.050	0.0171	0.0821	0.125

Table 7: $s = 6a_0$; ε_i = strain at plastic initiation; ε_{1f} = strain at first rupture; Δt = time delay to second rupture (ps).

For the [110]-orientation, on the other hand, ε_{1f} shows no tendency for an initial increase followed by a decrease as for the [100]-orientation but instead a decrease with end velocity is at hand. Also here a second rupture occurs at high enough end velocities. Only one case differs from the rest, namely $s = 12a_0$ at end velocity $v_{end} = v_0$. Here a first rupture occurs after a substantial elongation of the beam, with $\varepsilon_{1f} \approx 0.53$ and the second after an additional 0.275ps.

For both orientations hold that, as v_{end} increases, decisive necking regions eventual

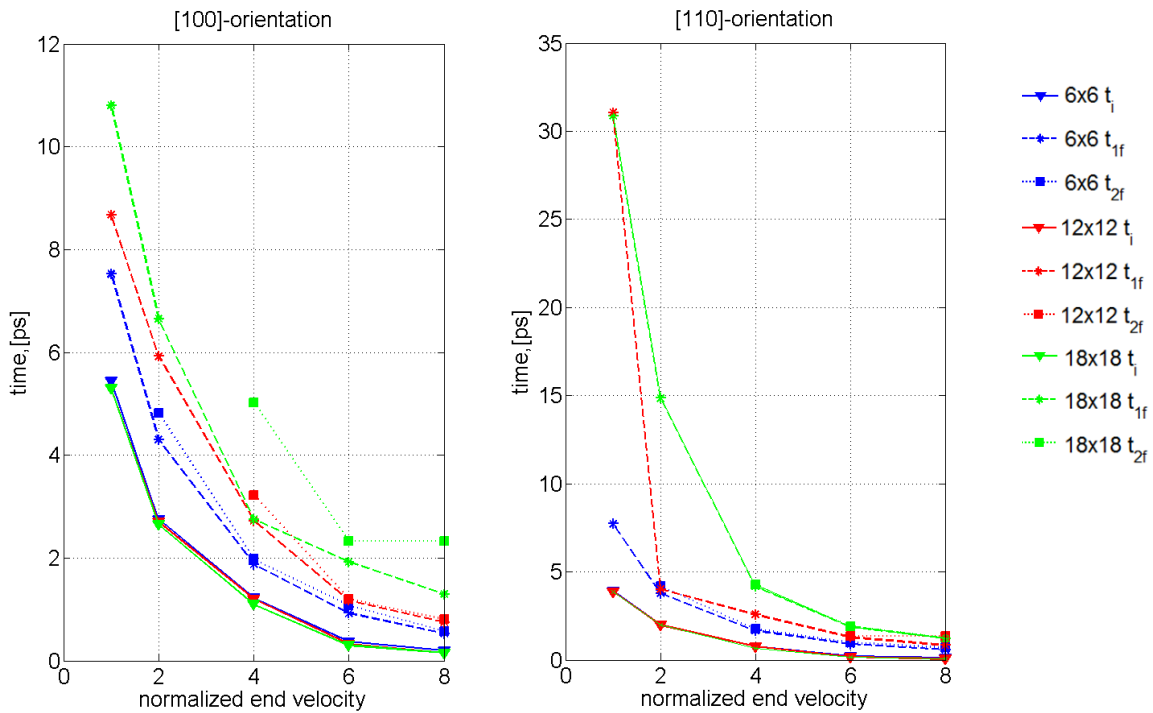


Figure 2: Time t_i , t_{1f} and t_{2f} versus normalized end velocity v_{end}/v_0 .

Orientation	[100]			[110]		
	ε_i	ε_{1f}	Second rupture, Δt	ε_{1f}	ε_{1f}	Second rupture, Δt
1	0.0911	0.1488	no	0.0667	0.5314	0.275
2	0.0932	0.2035	no	0.0684	0.1377	no
4	0.0838	0.1881	0.500	0.0547	0.1778	no
6	0.0359	0.1231	0.025	0.0205	0.1359	0.050
8	0.0239	0.1060	0.050	0.0103	0.1163	0.050

Table 8: $s = 12a_0$; ε_i = strain at plastic initiation; ε_{1f} = strain at first rupture; Δt = time delay to second rupture (ps).

Orientation	[100]			[110]		
	ε_i	ε_{1f}	Second rupture, Δt	ε_{1f}	ε_{1f}	Second rupture, Δt
1	0.0911	0.1847	no	0.0667	0.5284	no
2	0.0915	0.2283	no	0.0684	0.5087	no
4	0.0770	0.1898	2.275	0.0479	0.2873	0.075
6	0.0334	0.2001	0.400	0.0180	0.1949	0.025
8	0.0239	0.1813	0.175	0.0137	0.1710	0.050

Table 9: $s = 18a_0$; ε_i = strain at plastic initiation; ε_{1f} = strain at first rupture; Δt = time delay to second rupture (ps).

leading to rupture develops closer to the clamped ends whereas rupture occurs more centrally for low end velocities. Thus the chosen region of end velocities in the present investigations cover the transition between these two behaviors.

3.2 Stress-Strain curves

Also the stress-strain relations were recorded for all cases. The axial stress $\sigma_{x\parallel}$, with \parallel holding the crystallographic orientation, was determined as the mean stress in the axial direction calculated over all atoms in the beam. It was found that the stresses $\sigma_{x\parallel}^0$ at $\varepsilon_x = 0$, directly after relaxation of the beams, were non-zero and decreasing with increasing beam size for both orientations. In Figs. 2-5 the stress-strain curves, compensated for $\sigma_{x\parallel}^0$ so that they all pass through the origin, are shown for cross section side lengths $s = 6a_0$, $12a_0$ and $18a_0$, respectively, for different end velocities v_{end} and for both crystallographic orientations. The stresses at the vertical axes in Figs. 4-6 thus equals the exceed stress $\sigma_{x\parallel}^{exceed} = (\sigma_{x\parallel} - \sigma_{x\parallel}^0)$. The values of $\sigma_{x\parallel}^0$ are

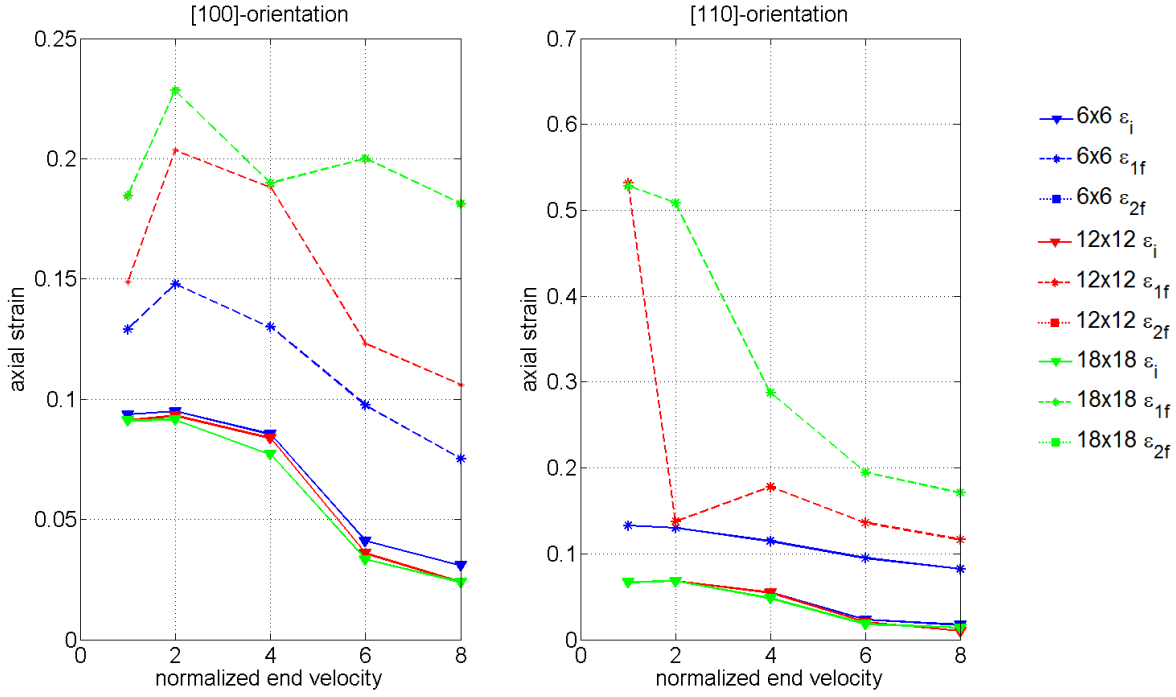


Figure 3: Applied axial strain ε_x versus normalized end velocity v_{end}/v_0 . ε_i = strain at plastic initiation; ε_{1f} = strain at first rupture, versus normalized end velocity v_{end}/v_0 .

given in Table 10. All curves in Figs. 4-6 are shown up to the point of first rupture strain ε_{1f} .

$s = 6a_0$	$s = 12a_0$	$s = 18a_0$
$\sigma_{x[100]}^0 = 1.37$	$\sigma_{x[100]}^0 = 0.679$	$\sigma_{x[100]}^0 = 0.462$
$\sigma_{x[110]}^0 = 1.28$	$\sigma_{x[110]}^0 = 0.710$	$\sigma_{x[110]}^0 = 0.521$

Table 10: Stress directly after relaxation (GPa).

As seen from the stress-strain curves the elastic behaviour is almost independent on end velocity for each orientation and for each size. Also, the elastic parts are nonlinear, most obvious for the [110]-orientation curves which are clearly convex. The [100]-orientation curves, on the other hand, are slightly concave. Thus the elastic behaviour is non-linear so that the modulus of elasticity varies with strain in addition to the well-known fact that it varies with size.

The first peak stress of each curve corresponds to the first dislocation formation, i.e. to plastic initiation, at strain ε_i . The yield stress is defined as the at which the material begins to deform plastically. Since the stresses $\sigma_{x\parallel}^0$ at $\varepsilon_x = 0$, directly after relaxation of the beams, were non-zero and decreasing with increasing beam size for both orientations, we introduce here the exceed yield stress, $\sigma_{Y\parallel}^{exceed}$, defined as

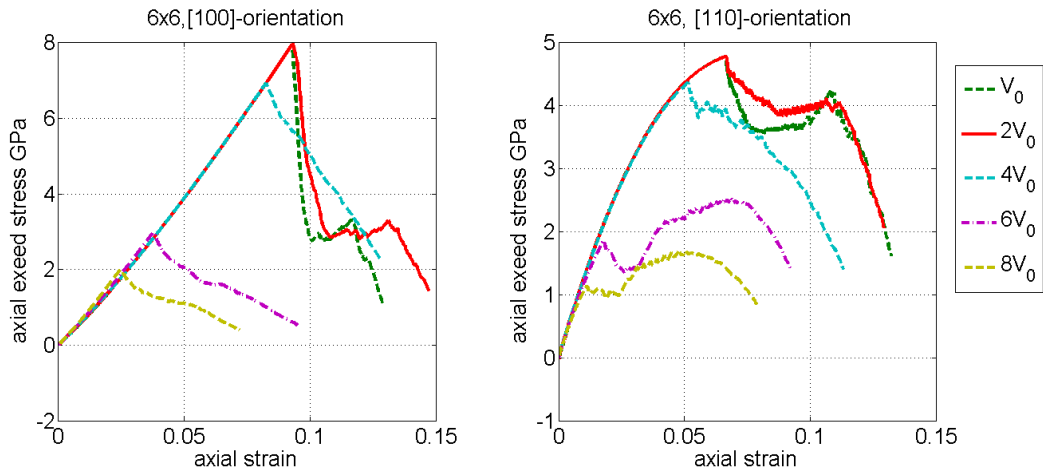


Figure 4: Axial exceed stress σ_x^{exceed} versus applied axial strain ε_x , $s = 6a_0$.

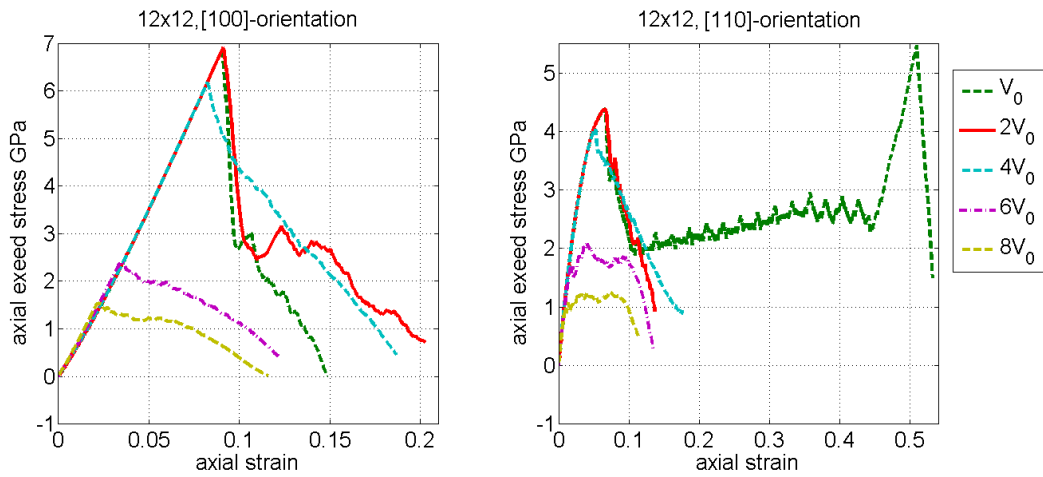


Figure 5: Axial exceed stress σ_x^{exceed} versus applied axial strain ε_x , $s = 12a_0$.

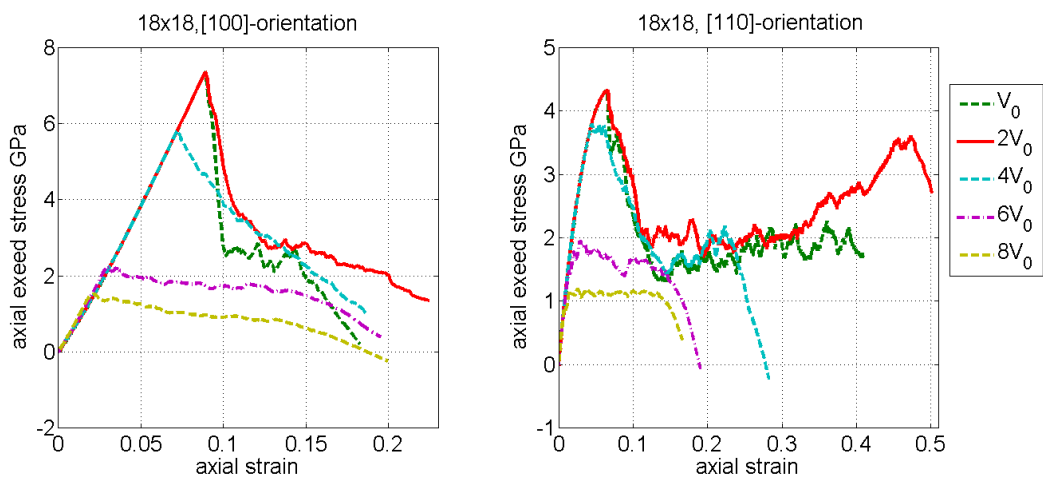


Figure 6: Axial exceed stress σ_x^{exceed} versus applied axial strain ε_x , $s = 18a_0$.

$\sigma_{Y\parallel}^{exceed} = (\sigma_{x\parallel}(\varepsilon_i) - \sigma_{x\parallel}^0)$, is given in Table 11 and plotted in Fig. 7. As seen, $\sigma_{Y\parallel}^{exceed}$ does not vary much with size but, on the other hand, there is a drop in magnitude of $\sigma_{x\parallel}^{exceed}$ between low and high end velocities, a factor of 3 – 4 for the velocity range investigated here. The shift starts as v_{end} exceeds $2v_0$. This holds for both orientations and all sizes.

M	1	2	4	6	8
$s = 6a_0$					
$\sigma_{Y[100]}^{exceed}$	7.95	7.98	6.98	3.14	2.13
$\sigma_{Y[110]}^{exceed}$	4.778	4.7794	4.43	1.96	1.31
$s = 12a_0$					
$\sigma_{Y[100]}^{exceed}$	7.95	7.98	6.98	3.14	2.13
$\sigma_{Y[110]}^{exceed}$	4.778	4.7794	4.43	1.96	1.31
$s = 18a_0$					
$\sigma_{Y[100]}^{exceed}$	7.95	7.98	6.98	3.14	2.13
$\sigma_{Y[110]}^{exceed}$	4.778	4.7794	4.43	1.96	1.31

Table 11: Stress directly after relaxation (GPa).

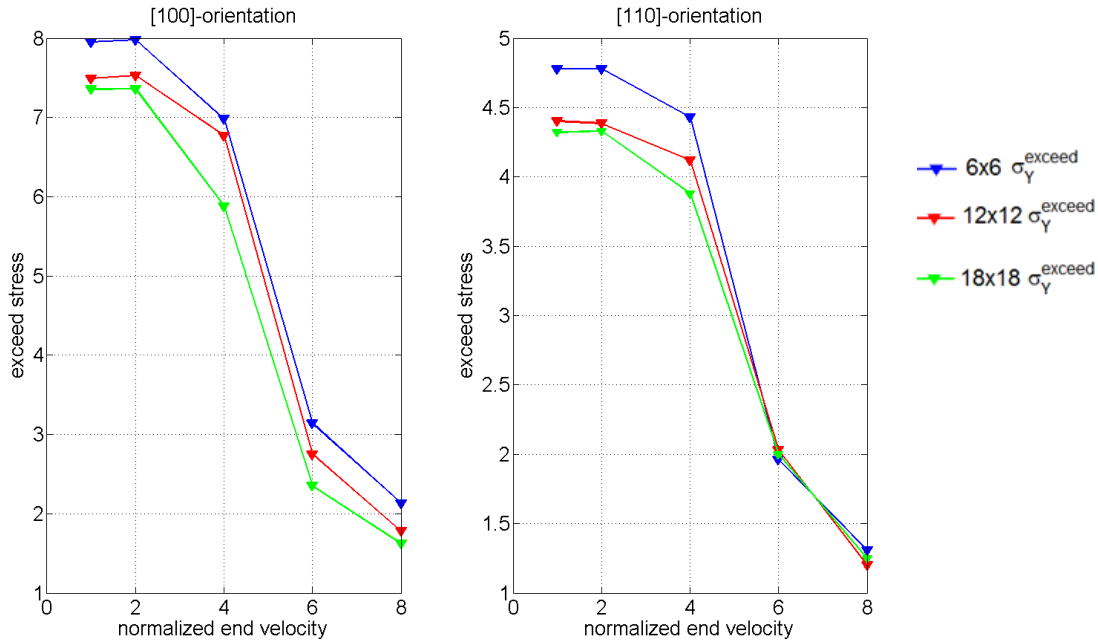


Figure 7: Exceed yield stress $\sigma_{Y\parallel}^{exceed}$ versus normalized end velocity v_{end}/v_0 .

3.3 Deformation developments patterns

How the plasticity in the beam develops and spreads depends on end velocity. After plastic initiation the plasticity spreads from the initiation spots into the still elastic parts of the beam through slip along preferred slip planes. This spread ceases more or less as neck formation starts depending on the velocity; at this point most of the slip events localize to the dominant necking regions and areas that still are elastic after final rupture remain so. If necking starts early in the loading process, as is the case if v_{end} is high enough, the beam has not elongated very much and corresponding rupture strain is low.

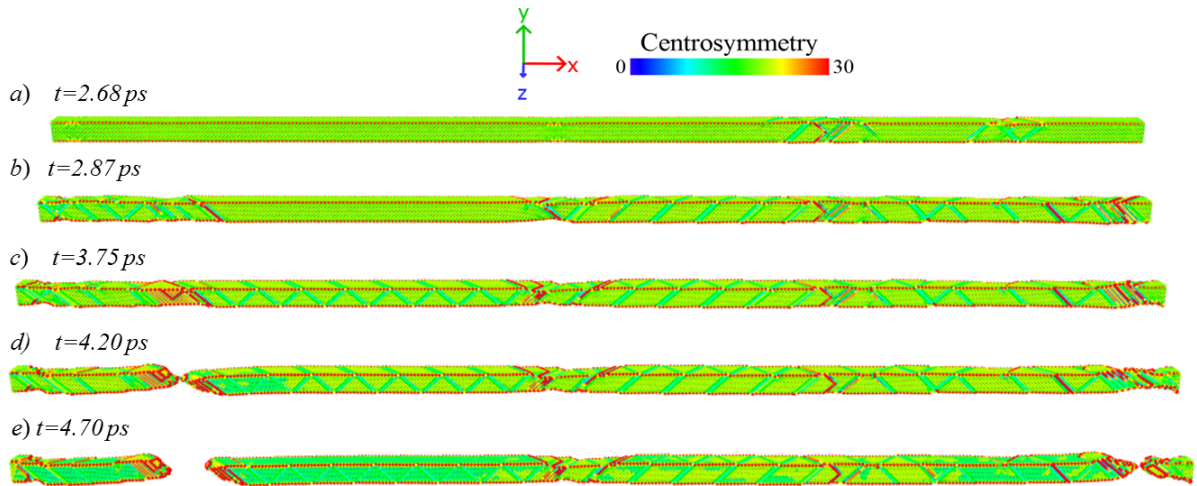


Figure 8: Snapshots of atomic arrangement along the curves in Fig. 4 for orientation [100] and velocity $2v_0$.

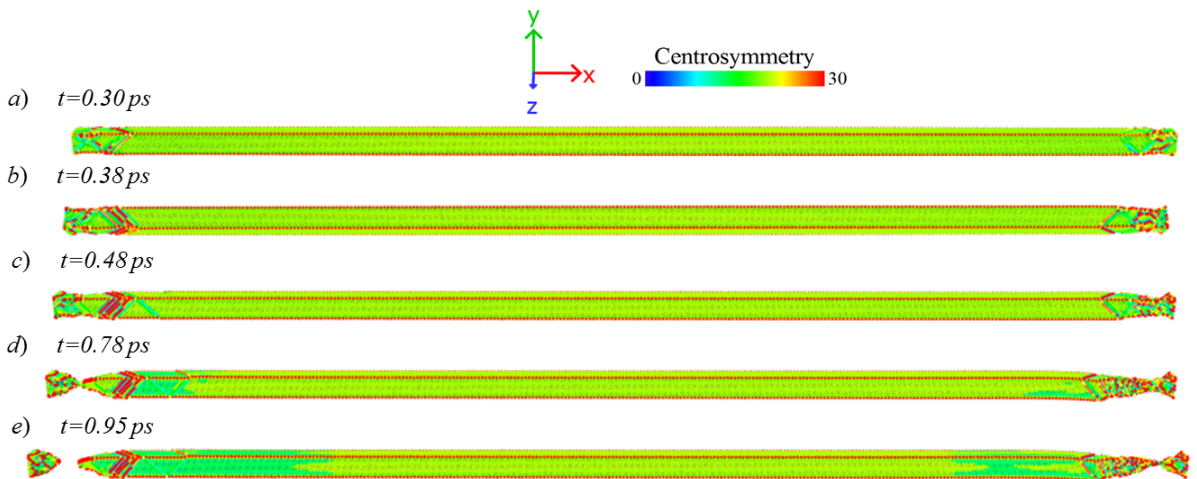


Figure 9: Snapshots of atomic arrangement along the curves in Fig. 4 for orientation [100] and velocity $6v_0$.

In Figs. 8-9 snapshots of the atomic arrangements for the [100]-orientation with end velocities $2v_0$ and $6v_0$, respectively, are shown, and in Figs. 10-11 the corresponding

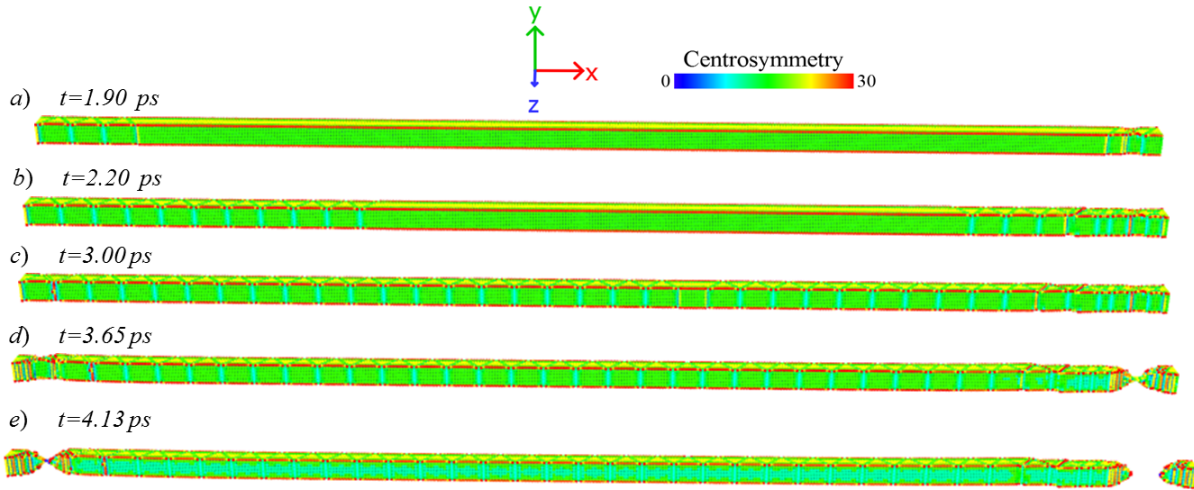


Figure 10: Snapshots of atomic arrangement along the curves in Fig. 4 for orientation [110] and velocity $2v_0$.

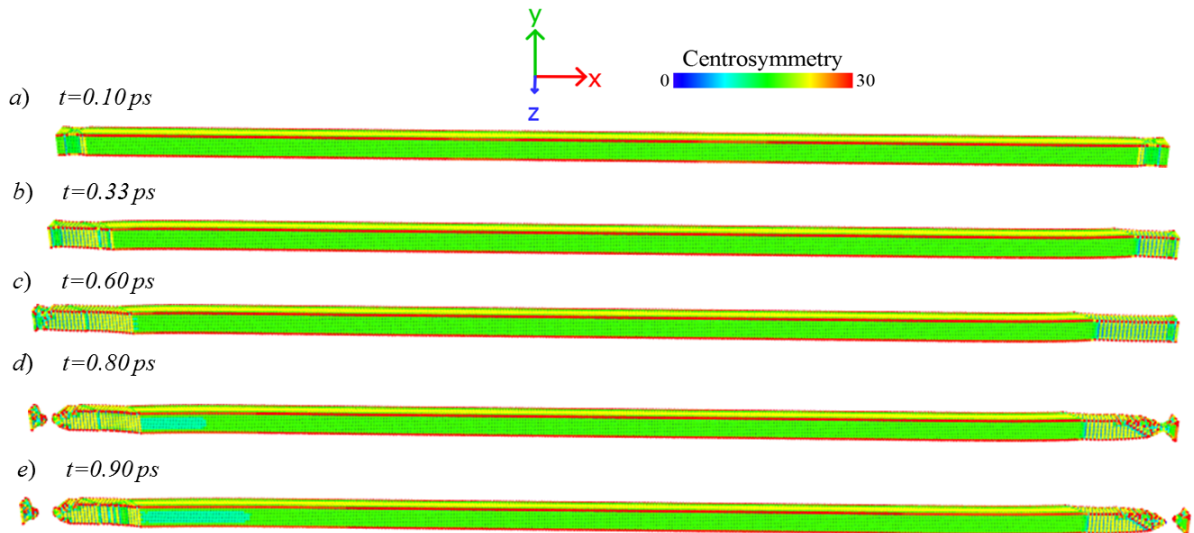


Figure 11: Snapshots of atomic arrangement along the curves in Fig. 4 for orientation [110] and velocity $6v_0$.

is shown for the [110]-orientation. Starting with [100]-orientation at low end velocity, $v_{end} = 2v_0$ shown in Fig. 8, it is seen that plasticity at time $t = 2.68$ ps, Fig. 8a), has initiated over three parts of the beam, with the most intense development about 25% of the beam length from the right end, and the weakest close to the left end. Following the snapshots over time, slip is seen to spread from the initiation sites into the elastic areas and new spots of high plastic deformation emerge. Eventually, for $t = 4.20$ ps as seen in Fig. 8d), rupture occurs at the distance of about 15% of the beam length from the left end, and this site is not one of the initial initiation sites from Fig. 8a). After this first rupture, relaxation of the beam starts from the rupture site but even so inertia causes a second rupture close to the right end at $t = 4.70$ ps, Fig. 8e). For the higher end velocity, $v_{end} = 6v_0$ and with snapshots shown in Fig. 9, the development is different. Plasticity concentrates close to both

ends and accumulates there. When first and second ruptures have occurred, Fig. 9e) at time $t = 0.95\text{ps}$, the central part of the beam is still elastic and unaffected by the loading. As for the [110]-orientation the events are different as seen in Fig. 10 for $v_{end} = 2v_0$ and in Fig. 11 for $v_{end} = 6v_0$. Initiation always occurs close to the beam ends, Figs. 10a)-11a), and the plasticity spreads towards the center of the beam. Before rupture in the case of $v_{end} = 2v_0$ the entire beam is affected by slip before two subsequent ruptures take place. For the high loading velocity with $v_{end} = 6v_0$ as seen in Fig. 11 the plasticity spread from the ends is limited, leaving most of the center of the beam in an elastic state after the last rupture.

4 Conclusions

Through molecular dynamics simulations the influence of loading rate on the mechanical response of tensile single crystal fcc Cu nano beams have been investigated. The beams had a constant length of $300a_0$, with a_0 denoting the lattice constant for Cu, and quadratic cross section with side length $6a_0$, $12a_0$ or $18a_0$. Two different crystallographic orientations, with loading in the [100] or the [110] directions, were considered. The beams were loaded by applying a constant velocity $v_{end} = Mv_0$, with $v_0 = a_0/400/\text{ps}$ and $M = 1, 2, 4, 6, 8$, to each end of the beam and the deformation pattern was followed in detail and the stress-strain curves recorded. It was shown that the elastic behavior of the beams was non-linear and, in practice, independent of size for each orientation. On the other hand the strain rate dependence was obvious. The strain at plastic initiation was found to be about three times higher for the lowest end velocities as compared to the highest, with the swap around $M = 4$. Also the yield stress was heavily reduced, by a factor of around three or four, above $M = 4$. The hardening behavior differed between the orientations. It was substantial for the [110]-orientation but not very pronounced for the [100]-orientation. This is due to the difference in slip patterns between the orientations. The symmetrical atomic arrangement for the [100]-orientation provides equal deformations over beam height and beam width, which induces an hourglass shaped necking region and from this rupture. This deformation pattern is not at hand for the [110]-orientation since the Poisson ratio is differs between the height and the width directions. Slip in this case causes a deformation pattern similar to that of when tilting a deck of playing cards along the loading direction. The arrangement allows for substantial elongations before a neck weak enough to rupture has been formed.

References

- [1] S. G. Nilsson and E. L. Sarwe and L. Montelius, Fabrication and mechanical characterization of ultrashort nanocantilevers, *Appl. Phys. Lett.*, **83**, 990–992, 2004.
- [2] S. G. Nilsson and X. Borrisñ and L. Montelius, Size effects on Youngys modulus of thin chromium cantilevers, *Appl. Phys. Lett.*, **85**, 3555–3557, 2004.

-
- [3] M. Hommel and O. Kraft, Deformation behavior of thin copper films on deformable substrates, *Acta Mater.*, **49**, 3935–3947, 2001.
- [4] R. Schweiger and G. Dehm and O. Kraft, Cyclic deformation of polychrystalline Cu films, *Phil. Mag.*, **83**, 693–710, 2003.
- [5] R. Schweiger and O. Kraft, Size effects in the fatigue behavior in thin Ag films, *Acta Mater.*, **51**, 195–206, 2003.
- [6] L. G. Zhou and H. C. Huang, Are surfaces elastically softer or stiffer?, *Appl. Phys. Lett.*, **84**, 1940, 2004.
- [7] A. Ahadi and S. Melin, Size dependence of the Poisson’s ration in single-crystal fcc copper nanobeams, *Comput. Mater. Sc.*, **11**, 322–327, 2016.
- [8] P. A. T. Olsson, S. Melin and C. Persson, Atomistic simulations of tensile and bending properties of single-crystal BCC-Iron nanobeams, *Phys. Rev. B*, **76**, 1–15, 2007.
- [9] P. A. T. Olsson and S. Melin., Atomistic studies of the elastic properties of metallic BCC nanowires and films, *Proc. IUTAM Symposium on Modelling Nanomaterials and Nanosystems*, **76**, 221–230, 2008.
- [10] LAMMPS, <http://lammmps.sandia.gov>.
- [11] A. Stukowski, Visualization and analysis of atomistic simulation data with OVITO-the Open Visualization Tool, *Modelling Simul. Mater. Sci. Eng.*, **18**, 2010.
- [12] B. L. Holian and A. F. Voter and N.J. Wagner and R.J. Ravelo and S. P. Chen and W. G. Hoover and C.G. Hoover and J. E. Hammerberg and T. D. Dontjie, Effects of pair-wise versus many-body forces on high-stress plastic deformation, *Phys. Rev. A*, **43**, 2655-2661, 1991.
- [13] B. L. Holian and R. Ravelo, Fracture simulations using large-scale molecular-dynamics, *Phys. Rev. B*, **51**, 11275-11288, 1995.
- [14] S. M. Foiles, M.I. Baskes and M.S. Daw, Embedded-atom-method functions for the fcc metals Cu, Ag, Au, Ni, Pd, Pt, and their alloys, *Phys. Rev. B*, **33**, 12–15, 1986.
- [15] B. T. Ellad and R. E. Miller, Modeling Materials Continuum, Atomistic and Multiscale Techniques, Cambridge University Press, 2011.
- [16] C. L. Kelchner and S. J. Plimpton and J. C. Hamilton, Dislocation nucleation and defect structure during surface indentation, *Phys. Rev. B*, **58**, 11085-8, 1998.
- [17] H. Y. Liang and G. R. Liu and X. Han, Computational Methods, Cambridge University Press, 2011.

- [18] P. Hansson, Influence of surface roughening on indentation behavior of thin copper coatings using a molecular dynamics approach, *Comput. Mater. Sc.*, **117**, 233–239, 2016.